Downhole Microseismic Source Location Based on a Multi-Dimensional DIRECT Algorithm for Unconventional Oil and Gas Reservoir Exploration

Qifeng YIN[1, *], Pengfei TAO[1], Shuo ZHENG[1], Qing HE[1], Yanfei AN[1] and Quanshi GUO[2]

1. *School of Resources and Environmental Engineering, Anhui University, Hefei 230601, China*
2. *Sinopec Geophysical Research Institute, Nanjing 211103, China*

Abstract: Because downhole microseismic data has the significant advantages of a high signal-to-noise ratio and well-developed P and S waves, the core and integral component of microseismic monitoring is to locate events with relatively high confidence level and accuracy associated with hydraulic fracturing, which is widely used for enhancing unconventional reservoir permeability and characterizing fractures. We present a multidimensional DIRECT inversion method for microseismic locations and applicability tests over modeling data based on a downhole microseismic monitoring system that has already been performed, proving the effectiveness of the proposed algorithm. In addition, synthetic tests also show that the location objective function can be defined into a multi-dimensional matrix space by employing the global optimization DIRECT algorithm, running without the initial value and the objective function derivation that makes use of a high searching density near the genuine solution but at a reduced density, as the objective points are scattered far away leading to an expeditious contraction of objective functions in each dimension. Finally, the DIRECT algorithm is extensively applied to real downhole microseismic monitoring data from hydraulic fracturing completions. The results show that the methodology based on a multidimensional DIRECT algorithm provides significant high accuracy and convergent efficiency as well as robust computation for interpretable spatiotemporal microseismic evolution, which is more suitable for real-time processing of large amounts of downhole microseismic monitoring data.

Key words: unconventional oil and gas reservoir, downhole microseismic monitoring, source location, DIRECT algorithm

E-mail: yinqifeng2005@163.com

1 Introduction

Hydraulic fracturing is of great significance for reservoir reconstruction and high-efficiency production of unconventional reservoir exploitation (Gu et al; 2015; Sun et al., 2015; Zou et al., 2015; Lin et al., 2016; Akram and Eaton, 2017; Zhu et al., 2017; Liu et al., 2018) and can stimulate thousands of microseismic events distributed around fracture networks. These events launch waves into the surrounding medium and they can be recorded by geophones installed in a borehole or near the surface (Zhang et al., 2013; Zhang et al., 2016; Meng et al., 2018). Associated with hydraulic fracturing processes, microseismic monitoring helps in understanding the geometric shapes of the induced fractures as well as resource characterization and estimation of the process effect of fracturing technology (Birialtsev et al., 2017; Woo and Kang, 2017; Soledad and Danilo, 2018; Alfataierge et al.,2019). In addition, the downhole microseismic monitoring we focus on in this work more approaches reservoirs, gaining wider recognition because of its advantages of a high signal-to-noise (S/N ratio), well developed P and S waves, and so on (Maxwell et al., 2010; Jones et al., 2014; Yuan and Li, 2017).

However, during these procedures, among the main objectives of microseismic monitoring is to accurately and expeditiously determine the position of each event (Soledad and Danilo, 2018; Zhuang et al., 2019). Thus, it was important in this study to develop an efficient algorithm that could not only automatically perform the detection and location of microseismic events in real time (Lagos et al., 2014; Soledad et al., 2018) but also efficiently process large amounts of actual data. For a long time, the linear inversion methodology based on the classical Geiger algorithm (Geiger, 1912) and the related location algorithms such as HYPO location series, host event location, double difference location (Waldhauser and Ellsworth, 2000; Zhang and Thunder, 2003), etc., could describe the microseismic source inversion in seeking the extremes of the objective function (Li et al., 2014), which effectively improves the locational accuracy but easily stretches into the local optimum and even results in a failed

inversion (Song et al., 2013). During recent years, the study of nonlinear intelligent algorithms for global optimization based on probabilistic selection preliminarily yielded very accurate microseismic inversion solutions (Zhu et al., 2015; Wang, 2016), including heuristic evolutionary algorithms (Simulated Annealing, Genetic Algorithm, etc.) (Lagos, 2014; Debotyam and Iraj, 2016) and random search algorithms (Pei et al., 2009). However, more often than not, these may not be practical for large amounts of microseismic event processing in real-time performance. In other words, it is extremely difficult to provide consideration to both locational accuracy and calculation efficiency (Zhu, 2015). In addition, the source scanning methodology working against event selection carries out the overall energy stacking in the time domain by meshing the solution space for the global optimization but it cannot fit a multi-parameter inversion of mass data because of the geometric growth of computation time caused by the mesh subdivision (Caffagni et al., 2016; Wang, 2016; Li et al.,2019). In the former cases, it is of paramount importance to select an appropriate method that involves weighing the advantages and disadvantages of all acceptable approaches in terms of accuracy requirements and computational limitations. Hence, we present the DIRECT algorithm proposed by Jones (1993) to detect microseismic events in this work. The results from Wang (2016) are consistent with Wei et al. (2012) in that the following searching zone in each iteration of the DIRECT algorithm will be determined by the function value of the sampling points as well as the subdivision of the hyperrectangles rather than calculating the derivative of the objective function (Peter, 2007; Wei et al., 2012). Furthermore, the implemented approaches, neglecting the detailed grid division, can seek an accurate and robust global optimal solution of a multivariable function as the derived solution space (Jones, 1993), where it searches for the objective points in a high density near the true solution but at a reduced density as they scatter far away, greatly improving data process efficiency and accuracy (Wang, 2016).

In practice, as a feasibility study, we implemented a borehole microseismic event simulation in the numerical modeling of an oil and gas reservoir by means of a ray tracing technique (Zhang, 2009; Song, 2012; Zhang, et al., 2016; Gao et al., 2017). As the velocity model and P-wave arrival times were derived, model tests showed the effectiveness of the multi-dimensional DIRECT inversion algorithm in recovering the location of the stimulated microseismic events. In addition, the extensive applications of the proposed methodology in actual microseismic monitoring data throughout hydraulic fracturing projects have been characterized by high locational accuracy and computational efficiency as well as significant applicability for real-time processing of microseismic monitoring with large amounts of data.

2 Geological Settings

The study area is located within Luntai County of Tahe oilfield, structurally the southeast slope of Akekule uplift in the middle region of Tarim Basin, Xinjiang Province (Fig. 1) (Liu et al.,2008; Zou et al., 2011). The Akekule uplift firstly formed in the mid to late Caledonian movement suffering regional compression in the early Hercynian movement with uplift into a large-scale arch trending northeast. The lower Ordovician suffered denudation, leading to the absence of the mid-upper Ordovician and Silurian-Devonian in most parts except only the surrounding slope area (Liu et al.,2008). Furthermore, regional geological surveys and studies have shown that the Tertiary strata covers on the top of this area, while the Ordovician strata is the bottom formation. Paleozoic clastic rack layers (S, D, C) are zone-by-zone overlying on the Ordovician strata (Zou et al., 2011).

As the largest basin in China, the Tarim Basin has large unconventional oil and gas resources potential (Zou et al., 2015; Lin, 2016; Liu et al., 2018). This study aims at providing the visual information of fractures development in both vertical and horizontal directions by microseismic location for the real-time monitor of fracturing work and corresponding adjustments during the unconventional tight gas productions. We applied the DIRECT locating technique to a downhole microseismic data set during one treatment stage along a vertical well. The layers involved in this project mainly are composed of three ascending stratigraphic units, the Yijianfang Formation (O_2yj), Bachu Formation (C_1b) and Kalashayi Formation (C_1kl) (Fig. 2) based on the good hydrocarbon evidence and commercial petroleum flow (Zhou et al., 2011). Associated with the dynamic monitoring of fractures induced by hydraulic fracturing in vertical well K1, within a horizontal distance of 569 m, a three-component 16-receiver array was laid out in another vertical monitoring well K2 with a detecting range of 5300–5450 m within a vertical space of 10 m, as shown in Fig. 2, where perforation shots were stimulated around 5495 m with approximately 295-g explosives. In addition, acquisition parameters were preset at a sampling interval 0.25 ms, dominant frequency of 500 Hz, and data record every 16 s. To evaluate the hydraulic fracturing process via scientific characterization of the geometric occurrence and development of fractures, we continuously maintained monitoring for 12 h throughout all of the fracturing stages.

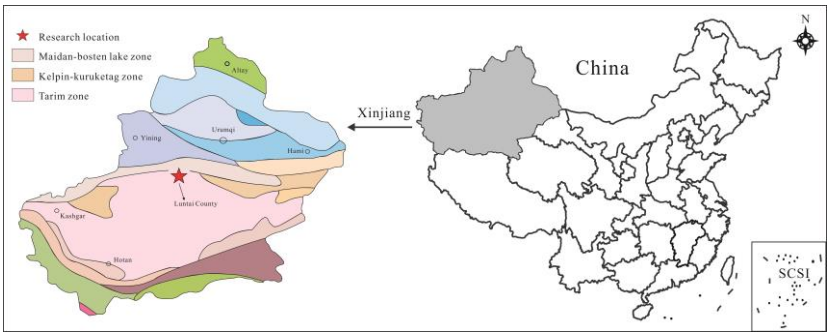

Fig. 1. Map showing the location and stratigraphic division in Luntai County of Tarim Basin, Xinjiang Province, China.

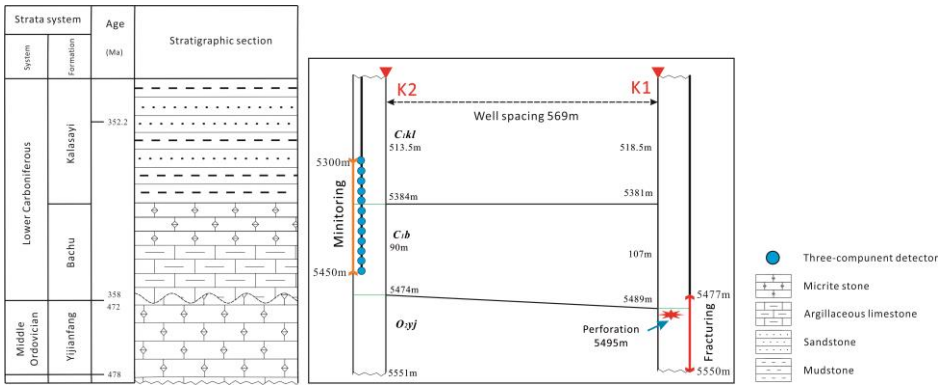

Fig. 2. Stratigraphic section of the study area and observational system of actual borehole microseismic monitoring. K1 is the fracturing well with the fracture range of 5477–5550 m; K2 shows monitoring well with a detecting range of 5300–5450 m. The horizontal distance between them is 569 m.

3 Methods

3.1 Microseismic monitoring technique

As described by Warpinski (2009), the general procedure of microseismic monitoring based on the theory of acoustics and kinematics (Zhu et al., 2017) does not differ from standard earthquake seismology principles (Zhao et al., 2017; Soledad and Danilo, 2018). As the reservoir pressure continuously increases during the process of hydraulic fracturing, a mass of microseismic events occur distributed around the fractures, emitting seismic waves composed of both P and S waves into the surrounding medium (see Fig. 3) that can be recorded for a few hours by geophones arranged in a borehole or near the surface (Song and Toksöz, 2011; Grechka et al., 2014; Li et al., 2019), as shown in Fig. 4, to detect the occurrence and development of microfractures. Compared to surface monitoring, the obvious advantage of downhole microseismic monitoring is that the detection is nearer the reservoir leading to a high S/N ratio, many more P and S waves, etc. for determining accurate event locations (Song et al., 2013; Chen et al., 2017; Hawthorne and Ampuero, 2017).

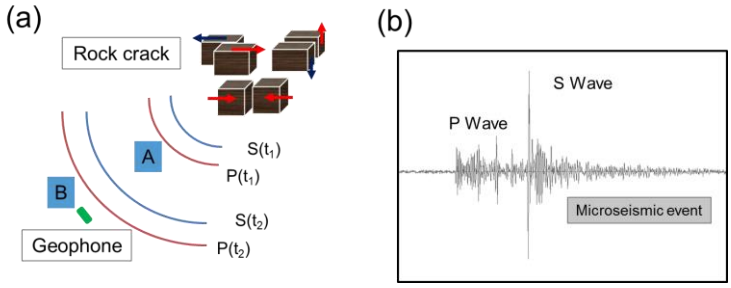

Fig. 3. Generation and propagation mechanism of microseismic waves (P and S waves).
(a) Waveforms of microseismic event. P/S waves propagate through point A in t1 and are received by geophones at point B in t2; (b) Single channel record of microseismic waves.

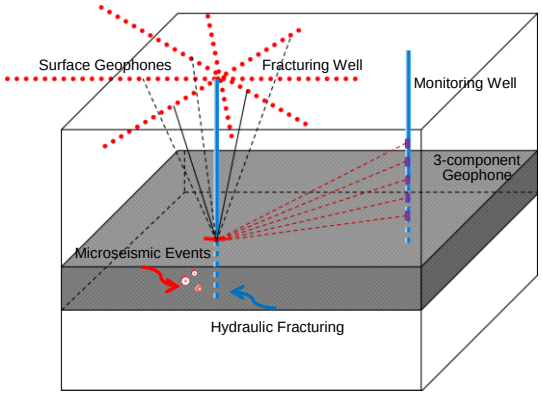

Fig. 4. Schematic diagram of downhole and surface microseismic monitoring observational system.

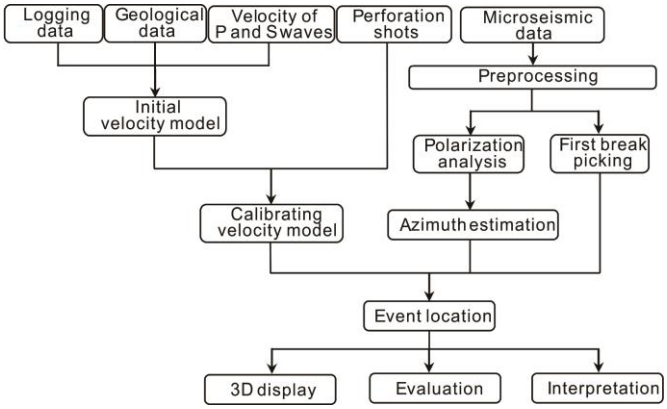

Fig. 5. Integrated flowchart describing the main processes leading to a microseismic event location.

Fig. 5 outlines the main processes of the workflow that leads to the location of a microseismic event. More broadly speaking, the relatively integrated procedures consist in identification of effective events on the microseismic records, selecting the arrival times of the P and S waves, deriving an approximate velocity model and source location that particularly is considered to be of paramount importance and a challenge in monitoring (Birialtsev et al., 2017; Soledad and Danilo, 2018). In other words, to better delineate fracture distribution, reliable locational algorithmic studies are extremely urgent. However, in many cases, we can only estimate the distance to the microseismic source from the difference between the P- and S-wave arrival times, while it is impossible to achieve the geometric shapes and original times of the events induced in a three-dimensional (3D) space (Soledad and Danilo, 2018; Chen et al., 2018) unless the direction where the energy originates from is determined using azimuth from the motion polarization analysis of both the P and S waves recorded by multistage three-component geophones (usually 12 or 16 pieces). As we focus on event location in this study, these preliminary works should already be completed.

3.2 DIRECT algorithm

A robust and efficient multi-dimensional Dividing RECTangles (DIRECT) algorithm (Gablonsky and Kelley, 2001) based on a grid search employing a one-dimensional (1D) Lipschitzian global optimization ideology described by Jones (1993) was used to help determine locations of microseismic events and make rapid decisions in the field. The DIRECT algorithm previously mentioned provides a detailed understanding of the global optimization problem for inversion as shown in Eq. (1) as follows:

$$f(x^*) = f^* = \min_{x \in \Omega} f(x) \tag{1}$$

where $\Omega = \left\{ x \in R^n \mid l_i \le x_i \le u_i \right\}$, $-\infty < l_i \le x_i < +\infty$, and the objective function $f(x)$ is Lipschitzian continuous in Ω (Jones, 1993). Generally, this approach consists in a several-step process in which the optimal hypermatrixes possibly existing will be first sought out in the searching space and then marked. A brief introduction of the optimizing steps follows (Chang et al., 2008):

1. We start by standardizing the objective zones into standardized hypercubes and then continuously

dividing them into smaller hypercubes and hyperrectangles at a size determined by the longest side of the hyperrectangle, whose center point indicates the objective function value;

2. The potential optimal hyperrectangle can be obtained after every iteration for further subdividing. Then, we select the one with the minimum function value as the potential optimal hyperrectangle for the next iteration if the divided hyperrectangles are of the same size; otherwise, the one with the maximum function value will be chosen if they are of the same function values.

3. We suppose m_i as the *i*-th central point and d_i (the distance from the central point to highest point) as the length of the hyperrectangle; then, the potential optimal hyperrectangle satisfies the following inequation:

$$f(m_j) - Kd_j \le f(m_i) - Kd_i \tag{2}$$

$$f(m_j) - Kd_j \le f_{\min} - \varepsilon \left| f_{\min} \right| \tag{3}$$

where $\varepsilon = 1 \times 10^{-4}$ is a positive constant as is typical and $f_{\min}$ is the current minimum function value. If L represents the longest side of the potential optimal hyperrectangle as I is the dimension set in this side, then

$$I_1 = \left\{ i \in I : d_i < d_j \right\} \tag{4}$$

$$I_2 = \left\{ i \in I : d_i > d_j \right\} \tag{5}$$

$$I_3 = \left\{ i \in I : d_i = d_j \right\} \tag{6}$$

where the interval of $j \in I$ is the potential optimal, if

$$f(m_j) \le f(m_i), \quad \forall i \in I_3 \tag{7}$$

Then, $K > 0$ occurs as follows:

$$\max_{i \in I_1} \frac{f(m_j) - f(m_i)}{d_j - d_i} \le K \le \min_{i \in I_2} \frac{f(m_i) - f(m_j)}{d_i - d_j} \tag{8}$$

$$\varepsilon \le \frac{f_{\min} - f(m_j)}{\left| f_{\min} \right|} + \frac{d_j}{\left| f_{\min} \right|} \min_{i \in I_2} \frac{f(m_i) - f(m_j)}{d_i - d_j}, \quad f_{\min} \ne 0 \tag{9}$$

$$f(m_j) \le d_j \frac{f(m_i) - f(m_j)}{d_i - d_j}, \quad f_{\min} = 0 \tag{10}$$

The hyperrectangular that satisfies the inequation (10) can be defined as the potential optimum for further division. In this case, for all $i \in I$, if *m* is assumed to be the central point of the hyperrectangle, the objective function will be sampled at $m \pm 1/3 L e_i$, where e_i is the *i*-th unit vector. The hyperrectangles can be first divided into a trisection along the direction of the minimum S_i dimension, where $S_i = \min(f(m \pm 1/3 L e_i))$; this process can be iteratively applied to a secondary minimum S_i dimension until all the directions are completely performed. For this reason, the studied method ensures global convergence in every dimension because it always divides the hyperrectangles from the longest dimension (Chang et al., 2008; Wei et al., 2012).

More specifically, Fig. 6 shows a schematic diagram of the first three iterations using the DIRECT algorithm in two-dimensional (2D) space $f(x,z)$, where the objective function values are labeled as black dots and the potential optimal rectangles are shaded. As shown in Fig. 6a, the potential optimal matrix is assumed to be a square region with an objective function value $f = 8$ scattering at the center, where four points are sampled to calculate the objective function during the first iteration. Considering the scenarios $S_1 = \min(2,6) = 2$, $S_2 = \min(4,7) = 4$, and $S_1 < S_2$, the initial rectangle is certainly divided into a trisection along the Z direction (the longest side) and then a similar behavior is iterated to the middle rectangle in the X direction. Thus, five potential optimal rectangles are obtained (see Fig. 6a) by means of a DECRT strategy that provides a maximum space to the minimum function value. Fig. 6b shows that a new definition of a potential optimal rectangle, which is of a small size at the bottom with a new minimum value $f = 2$, is also divided into trisection along the longest side (*x* direction) as in the theory previously described. As the third iteration produces two potential optimal rectangles whose function values are equal to the ratio of the two maximum sides in Fig. 6c, the sampling and dividing

maintains in carrying out, respectively, as is typical and so on until all the minimum values are obtained. Benefiting from the aforementioned division strategy, in a limiting case, the whole object region will be divided into infinite rectangles generating a dense solution space, as well as the particularity of the global convergence in every dimension, which provides great confidence not only to guarantee global convergence in the microseismic location but also more efficiency and accuracy (Gablonsky and Kelley, 2001; Chang et al., 2008; Wang, 2016).

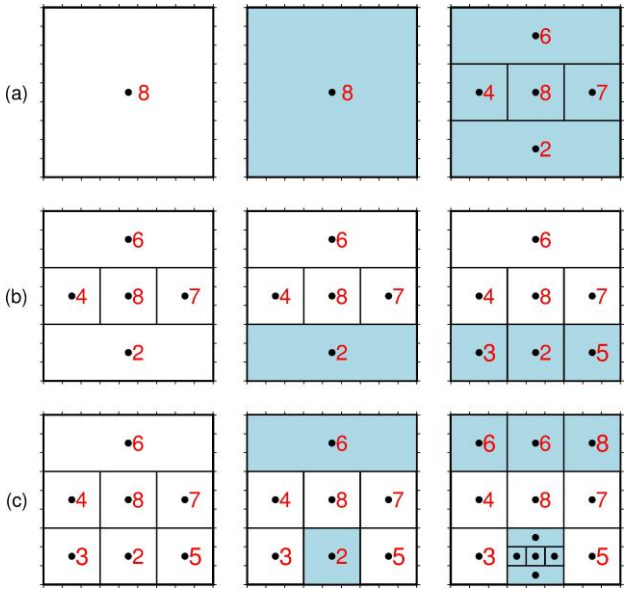

Fig. 6. 2D schematic diagram of the first three iterations using the DIRECT algorithm.
Black dots represent the central points of the hyperrectangle; Red figures are the objective function values.

4 Results

4.1 Model test and analysis

To investigate the accuracy and efficiency of implementing the multi-dimensional DIRECT algorithm, we generated a suite of geological models consisting of nine homogeneous flat layers of a size of 1000×1000 m, as shown in Fig. 7, where the fracturing well S1 and receiving well S2 were both designed at positions of 300 m and 700 m, respectively. Moreover, a vertical array of 12 downhole geophones was modeled using a channel spacing of 10 m from 5250 m to 5360 m for receiving the synthetic travel times and ray paths of the microseismic event induced by the fracturing project, which was also simulated ranging from 5450 m to 5550 m in the model. On the basis of actual logging data, Fig. 8 shows the nine-layer vertical P-wave velocity model for the oil-gas reservoir model above.

To explore the locational approach accuracy, a microseismic event was supposed to stimulate at (300 m, 5500 m) using a ricker wavelet with a dominant frequency of 100 Hz and the parameters of acquisition included a sampling interval of 0.25 ms and a record length of 0.5 s. In this case, only P-wave first arrivals (direct or head wave) were used for the test; hence, Fig. 9 shows the record obtained from ray tracing, and the first break selected by the blocky Short Time Average over Long Time Average (STA/LTA) curves is provided in Table 1.

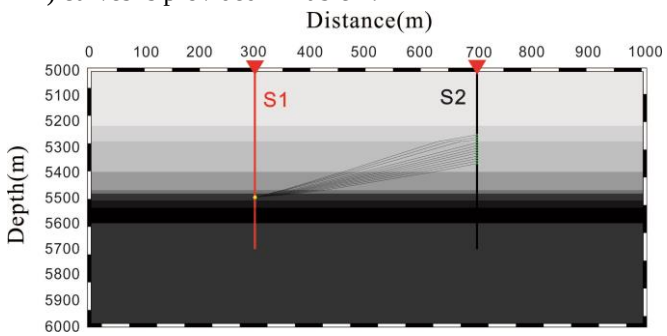

Fig. 7. Downhole microseismic monitoring in a layered geological model for the synthetic test.
Green circles represent the geophones in the monitoring well S2 and yellow stars denote microseismic events in well S2; Black lines represent microseismic wave ray paths; The horizontal distance between source and geophone array is 300 m.

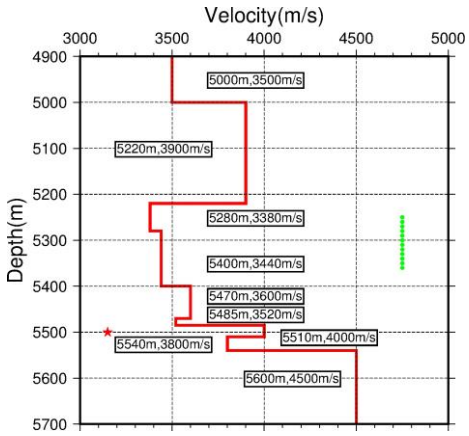

Fig. 8. P-wave velocity model of the oil-gas reservoir used in the microseismic simulation.
The red star symbol on the left represents the relative depth of the microseismic source; The circle symbols on the right show the relative depth of 12 geophones.

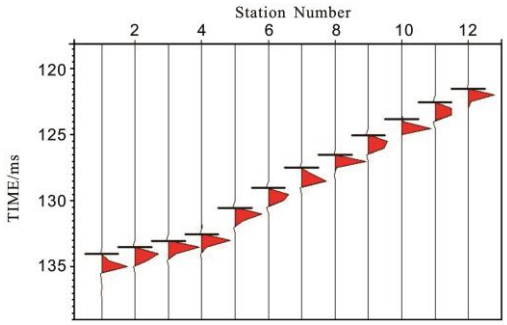

Fig. 9. First break selecting of P wave on microseismic simulation record.
The black lines indicate the P wave arrival.

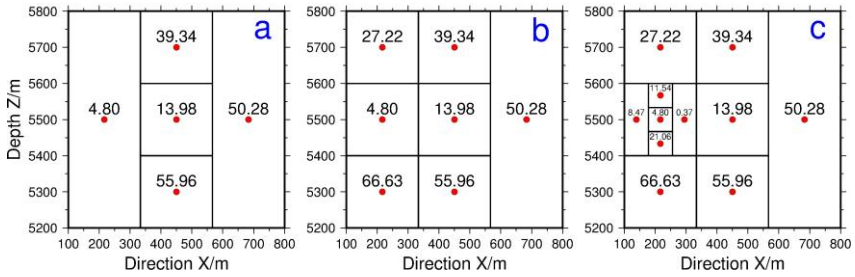

Fig. 10. Rectangle division form and objective function value during the first three iterations.
Red dots represent the central points of the hyperrectangle; Black figures are the objective function values: (a) first iteration; (b) second iteration; (c) third iteration.

Table 1 Coordinates and first break times of 12 receivers

Station	*X*(m)	*Z*(m)	First break(ms)
1	700	5250	134.00
2	700	5260	133.52
3	700	5270	133.03
4	700	5280	132.53
5	700	5290	130.53
6	700	5300	129.02
7	700	5310	127.50
8	700	5320	126.54
9	700	5330	125.01
10	700	5340	123.79
11	700	5350	122.51
12	700	5360	121.53

Because the DIRECT algorithm we present is also a selection-based approach, the microseismic event location requires determination of the differences between P-wave arrival times, which can be regarded as the objective function of the rectangle center. As the velocity model (Table 1) and first break times (Table 2) were available during preliminary processing, we located an event on a 2D plane of *x*-*z* using the DIRECT algorithm for the distance to the microseismic source. Before the first iteration, we set an enlarged initial rectangular region $x \in [100,800]$, $z \in [5200,5800]$ for the whole search space, which can be estimated according to the forward model as well as perforation shots or geological data in practice. Fig. 10 shows the rectangle division forms and objective function values of the model location during the first three iterations, agreeing well with the distributing characteristics shown in Fig. 6. The iteration was repeated 200 times until a stop criterion was reached for the successful achievement of a final location at (299.42 m5500.23 m) with the optimal travel time difference of 7.42×10^{-3} ms. To facilitate analysis, Fig. 11 shows an overview of the searching path (red cross symbols) and the final location (blue square symbol) of the inversion, which completely shows the characteristics of a high-density search near the true solution but reduced search density away from the true solution.

For further analysis of the convergence rate and locational accuracy, Fig. 12 shows the projection distribution of the objective function values after each iteration in the Z (Fig. 12a) and X (Fig. 12b) direction, respectively. Zooming up the red portions of Fig. 12a and b for a distinct observation as shown in Fig. 12A and B, one can more evidently see the optimal solution at Z=5500.53 m and X=299.42 m. Combined with the spatial distribution of travel time differences shown in Fig. 13, the general trend of improving convergence rate for each dimension and global optimization using the DIRECT algorithm can be clearly seen. As expected, we never provided the initial value or calculated the derivative of the objective function even with a wider search space when the location inversion was performed. All the aforementioned signs indicate that the methodology we present is effective in obtaining more accurate event locations and deserves broader application.

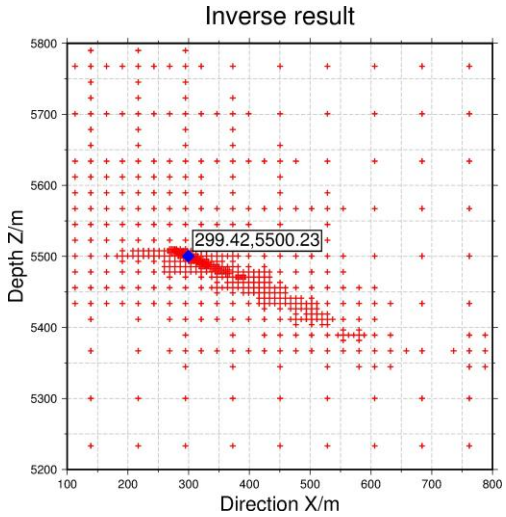

Fig. 11. Searching path (red cross symbols) and final location (blue square symbol) of the DIRECT algorithm.

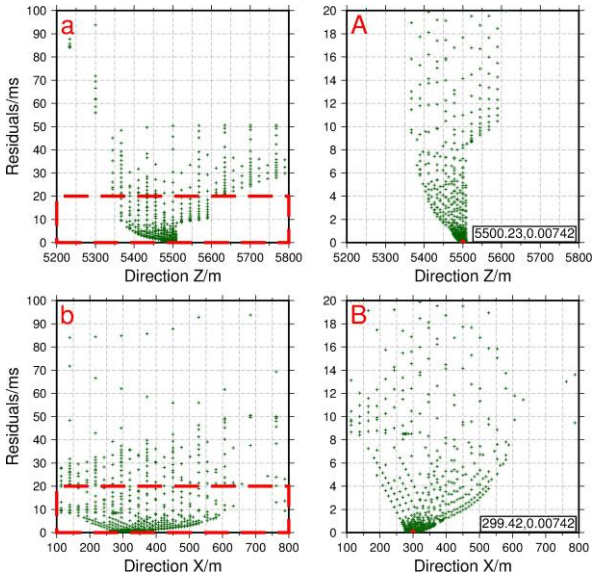

Fig. 12. Inversion results using the DIRECT algorithm in the X and Z directions.
Green cross symbols represent the objective function values; Red symbol shows the final location; (a) objective function value positions in the Z direction; (b) objective function value positions in the X direction; (A) and (B) Zoomed-in plots.

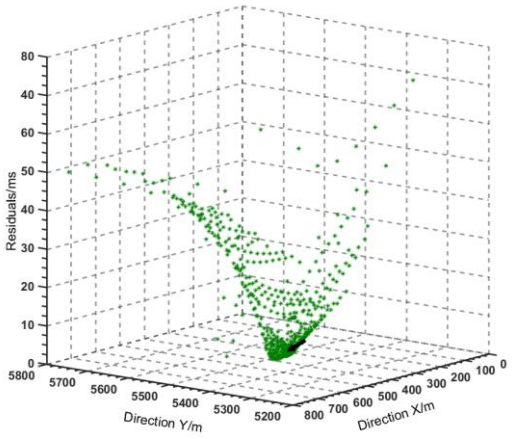

Fig. 13. Inversion results in 3D space using the DIRECT algorithm.
Green cross symbols represent the time residuals of the objective function.

4.2 Microseismicity Spatial Distribution of Field data Set

The continuous downhole data set was processed with the DIRECT inversion algorithm over the course of treatment project. As for the locational problem, which constitutes the main objective of this work, we required the optimization of the DIRECT algorithm as well as reasonable estimation of the velocity model and accuracy of the P- or S-wave arrival times as previously mentioned. In this case, we could first derive an approximate velocity model according to the well sonic log data (black dotted line shown in Fig. 14) involving the monitoring geophone layers and hydraulic fracturing, which can be well recovered into a new calibrated velocity model as in the red line shown in Fig. 14. Meanwhile, the difference between the P-wave arrival times could also be obtained from the best Z component selections on the separate three-component records of the identified effective events as shown in Fig. 15 for reference.

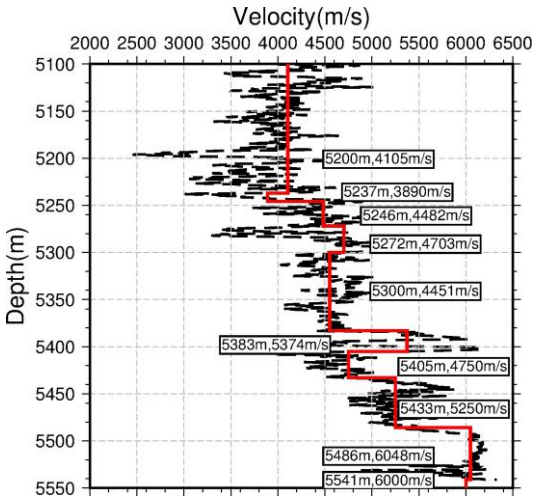

Fig. 14. Inversion velocity model (red line) for actual data.
The black dotted line represents well sonic log data.

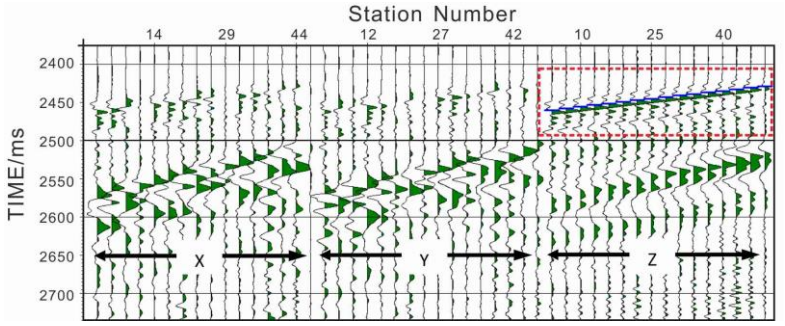

Fig. 15. Three-component records (separated into X, Y, and Z) of a certain effective event.
Blue lines show the first break times of the P wave.

Because the position and origin time of the perforation shot is known, it is generally used to estimate an inversion method suitable for real-time microseismic location. Thus, we performed a precision test case based on the velocity model as well as the aforementioned first break times for the perforation shot location on a 2D plane of R-Z, where the R-axis is a horizontal line crossing both wells K2 and K1 and the Z-axis denotes the depth direction. For convenient calculation, we set the wellhead coordinate of K2 at (0, 0) and K1 at (569, 0) and then the perforation shot position was expressed as (569, 5495). Consequently, the inversion calculation was conducted using the aforementioned proposed methodology with a final location at (562, 5490), very near the actual perforation shot. In fact, the same methodology and parameters have been adopted to address the actual data of downhole microseismic monitoring leading to an expected result. To facilitate analysis, Fig. 16 shows the results of the 2D location corresponding to the whole hydraulic fracturing, where a, c, e, and g are top view maps; b, d, f and h are side view maps; and the color indicates the time of the microseismic events generated and the uniform size represents the energy difference.

Finally, we needed to estimate the hydraulic fracturing process and fracture development according to the microseismic locational results during different stages (as shown in Fig. 16). Fig. 16a and b show the beginning stage S-1 of the fracture filling, where the microseismic events mainly induced by rock tension appear to be of weak energy because of the lower stratum pressure and higher fracturing fluid leak-off. As a result, the events generated at this moment are gathering around the fracturing well K1 at a low density. As the fracturing work continues, there is a significant rupture of argillaceous rock referring to geological data at the mid-section because of a continuous increase in stratum pressure, agreeing well with the microseismic locational results of stage S-2 shown in Fig. 16c and 16d. Abnormally, although stage S-3 processes are depressurized and of reduced emission, the events in contrast increase and strengthen, forming a fracture group F1 along a NE direction as shown in Fig. 16e and 16f. At the termination of pumping, argillaceous fracture groups tend to stop, but there was further development of fracture groups in carbonate rocks composed of a small one F2 far from K1, F3 along a NE direction, and F4 along an ESE direction as shown in in Fig. 16g and 16h. As expected, the microseismic events present an apparent hysteresis because of the increasing fracture closure pressure with the cessation of fracturing. According to the density distribution of the located microseismic events using the DIRECT algorithm and the formation order of fracture groups, we could make reasonably interpret the fracturing process as Fig. 17 shown. Table 2 summarizes the spatial parameters

of the four fracture groups including F1, F2, F3, and F4.

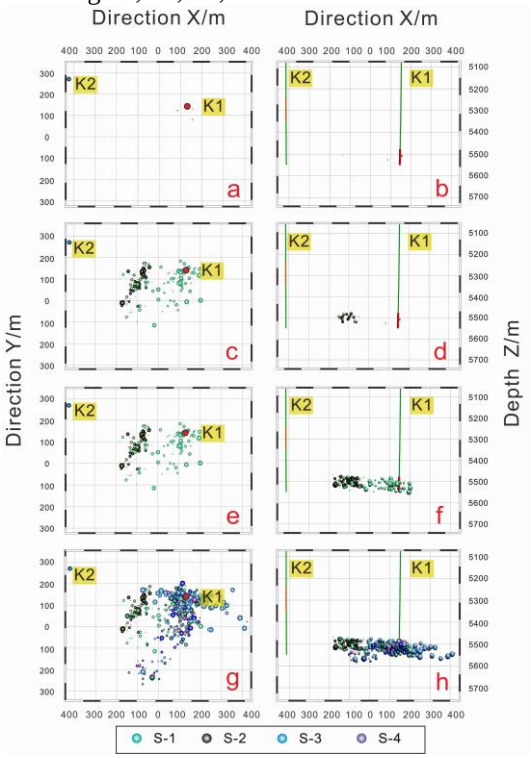

Fig. 16. Locations of borehole microseismic events during different stages. a, c, e, and g are top view maps. b, d, f, and h are side view maps.

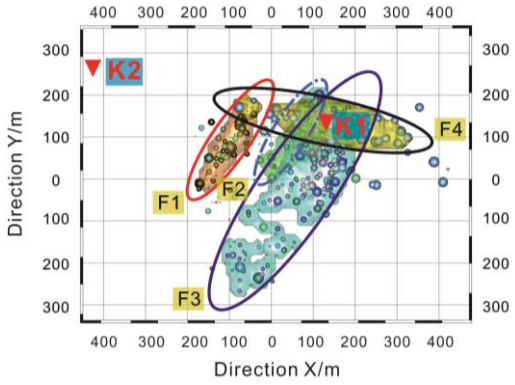

Fig. 17. Fracture group interpretation of borehole microseismic events.

Table 2 Spatial parameters of fracture groups

Fracture	Events	Length(m)	Height (m)	Width (m)	Dip (°)	Volume (10^3m^3)
F1	47	232.248	53.882	45.464	N33E	253.323
F2	50	339.26	110.765	59.749	N37E	867.371
F3	60	473.738	143.642	105.943	N26E	2004.640
F4	78	485.608	96.345	76.683	E13S	1110.805

5 Discussions

Microseismic monitoring has been the primary technology to diagnose the efficiency of hydraulic fracturing processes in unconventional reservoir exploitation (Maxwell et al., 2010; Zhu et al., 2017; Liu et al., 2018). Conventional location approaches exist, such as linear inversion (Geiger, 1912), that seem to be very efficient as they provide computationally fast solutions, but they have substantial disadvantages of local convergence and yielding an initial value. In contrast, nonlinear methods have

global optimization capability, but at the expense of slower computational times because of a large number of inversion parameters (Debotyam and Iraj, 2016; Wang, 2016; Soledad and Danilo, 2018). Our work focused on developing robust and efficient algorithms capable of expeditiously processing large amounts of microseismic events in real time, aiding in making rapid decisions in the field.

The proposed DIRECT algorithm is a global optimization technique based on a grid search (GS) (Peter, 2007; Wei et al., 2012; Tan et al., 2017) requiring reliable arrival times as well as a velocity model and has been proven to be robust and efficient in determining hypocentral locations. Compared to a classical GS, in the case of given solution space, the DIRECT implementation is more suitable for optimizing a global solution of multivariate functions as the following searching zone in each iteration of the DIRECT algorithm is determined neither by an explicit objective function or a derivative equation, but rather by a function value of sampling points as well as subdivision of hyperrectangles. Thus, there is a high density of objective points near the genuine solution but in a reduced density as they scatter afar (Fig. 13), showing the advantages of using DIRECT over GS to attain significant speed-ups.

We further tested the efficiency of our DIRECT-based method by comparing it to the standard GS algorithm. Fig. 18 shows a 3D display of all the grid search points and time residuals by GS from the same model shown in Fig. 7. As shown, we have to search for each point in the whole space already meshed to determine the global optimal solution, which could increase of the extent of calculation. In addition, the inversion accuracy and reliability of GS depends heavily on the mesh size; a smaller results in higher precision but longer computational times. For each event location, statistics demonstrated that only 0.03 s was spent for 200 iterations using the DIRECT method with a grid 5 m × 5 m and a searching range of 700 m × 600 m, but 2 s for 2500 iterations using the traditional grid search method using the same grid and searching range of 300 m × 300 m. Thus, the DIRECT algorithm is particularly suitable for multi-event, multi-parameter microseismic inversion in a large-scale space with the advantages of shorter search times and higher accuracy.

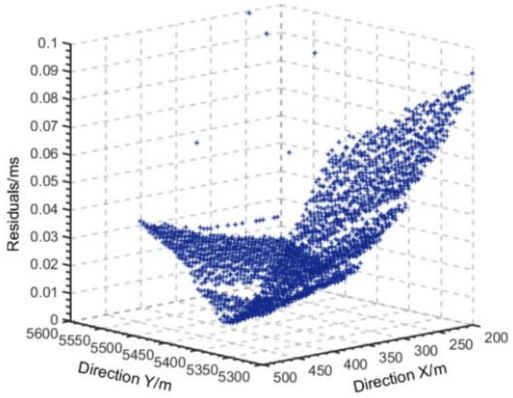

Fig. 18. Inversion results in 3-D space by grid search (GS).
Blue cross symbols represent the time residuals of objective function.

6 Conclusions

(1) Downhole microseismic monitoring with the main objective of event location has numerous applications in unconventional reservoir characterization and exploitation, which is of great interest not only to appraise hydraulic fracturing projects and fracture treatment, but also to avoid potential natural hazards.

(2) Aiming for more effective event location, we proposed a global optimization method to process borehole microseismic data using the DIRECT algorithm. Compared to classical inversion methodologies, this new method is more robust and accurate and can effectively solve the problems that have been puzzling for a long time such as local convergence and a slow operating rate.

(3) Both theory tests and field data application demonstrate the DIRECT algorithm's feasibility in determining locations for downhole microseismic monitoring, neglecting an initial value and applying an objective function derivation. The process uses a high searching density near the genuine solution but a reduced density as the points scatter afar, leading to an improved convergence rate for each dimension and global optimization during iterations. In brief, because of its accuracy and effectiveness, the DIRECT algorithm method can be used with relatively high confidence to process large amounts of downhole microseismic monitoring data in real time.

Acknowledgments

The implementation of the study benefited from the great help of Guoshu Cui from Sinopec Geophysical Research Institute. And we thank the anonymous reviewers and the editors for their

suggestions. This research was supported by the National Natural Science Foundation of China (Grant No. 41807296 and No. 41802006), Natural science found for universities of Anhui province (Grant No. KJ2017A036).

References

Akram, J., and Eaton, D.W., 2017. 1D layered velocity models and microseismic event locations: synthetic examples for a case with a single linear receiver array. *Journal of Geophysics and Engineering*, 14(5):1215–1224.

Alfataierge, A., Miskimins, J.L., Davis, T.L., and Benson, R.D., 2019. 3D Hydraulic-Fracture Simulation Integrated With 4D Time-Lapse Multicomponent Seismic and Microseismic Interpretations, Wattenberg Field, Colorado. *SPE Production & Operations*, 34(1):57 – 71.

Birialtsev, E.V., Demidov, D.E., and Mokshin, E.V., 2017. Determination of moment tensor and location of microseismic events under conditions of highly correlated noise based on the maximum likelihood method. *Geophysical Prospecting*, 65(6): 1510–1526.

Caffagni, E., Eaton, D. W., Jones, J. P., and Baan, M.V.D., 2016. Detection and analysis of microseismic events using a matched filtering algorithm (MFA). *Geophysical Journal International*, 206(1):ggw168–ggw658.

Chang, Y.Z., ·Hung, K.T.,·and Lee, S.T., 2008. Human face detection with neural networks and the DIRECT algorithm. *Artificial Life and Robotics*, 12 (1-2):112–115.

Chen, H.C.,, Meng, X.B., Niu, F.L., and Tang, Y.C., 2018. Microseismic Monitoring of Stimulating Shale Gas Reservoir in SW China: 2. Spatial Clustering Controlled by the Preexisting Faults and Fractures. *Journal of Geophysical Research-Solid Earth*, 123(2):1659–1672.

Chen, Y.K., Zhang, H.J., Miao, Y.Y., Zhang, Y.S., and Liu, Q., 2017. Back azimuth constrained double-difference seismic location and tomography for downhole microseismic monitoring. *Physics of the Earth and Planetary Interiors*, 264:35–46.

Debotyam, M., and Iraj, S., 2016. Neuro-evolutionary event detection technique for downhole microseismic surveys. *Computers & Geosciences*, 86: 23-33.

Gablonsky, J.M., and Kelley, C.T., 2001. A locally-biased form of the DIRECT algorithm. *Journal of Global Optimization*, 21: 27–37.

Gao. J., and Zhang, H.J., 2017. An efficient joint inversion strategy for 3D seismic travel time and DC resistivity data based on cross-gradient structure constraint. *Chinese Journal of Geophysics*, 60(9): 3628–3641.

Geiger, L., 1912. Probability method for the determination of earthquake epicenters from the arrival time only(translated from Geiger's 1910German article). *Bulletin of St. Louis University*, 8(1):56–71.

Grechka, V., and Yaskevich, S., 2014. Azimuthal Anisotropy in Microseismic Monitoring: A Bakken Case Study. *Geophysics*, 79(1): KS1–KS12.

Gu, M.W., Lu, S.F., Xiao, D.S., Guo, S.Q., and Zhang, L.C., 2015. Present Situation of Core Mercury Injection Technology of Unconventional Oil and Gas Reservoir. *Acta Geologica Sinica* (English edition), 89(z1):388-389.

Hawthorne, J.C., and Ampuero, J.P., 2017. A phase coherence approach to identifying co-located earthquakes and tremor. *Geophysical Journal International*, 209, 623–642.

Jones, D.R., Perttunen, C.D., and Stuckman, B.E., 1993. Lipschitz optimization without Lipschitz constant. *Journal of Optimization Theory and Application*. 79(1):157–181.

Jones, G.A., Kendall, J.M., Bastow, I.D., and Raymer, D.G., 2014. Locating Microseismic Events Using Borehole Data. *Geophysical Prospecting*, 62(1): 34–49.

Lagos, S.R., Sabbione, J.I., and Velis, D.R., 2014. Very fast simulated annealing and particle swarm optimization for microseismic event location. Expanded Abstracts. *Society of Exploration Geophysicists*, 2188–2192.

Li, J., Gao, Y.T., Xie, Y.L., Zhou, Y., and Yang, K., 2014. Improvement of microseism locating based on simplex method without velocity measuring. *Chinese Journal of Rock Mechanics and Engineering*, 33(7):1336–1345.

Li, L., Tan, J.Q., Xie, Y.J., Tan, Y.Y., Walda, J., Zhao, Z.G., and Gajewski, D., 2019. Waveform-based microseismic location using stochastic optimization algorithms: A parameter tuning workflow. *Computers & Geosciences*, 124:115 – 127.

Li, M., Li, H.F., Tao, G., Ali, M., and Guo, Y.H., 2019. Microseismic event location using multi-scale time reversed imaging. *Journal Of Petroleum Science And Engineering*, 174: 144 – 160.

Lin, W., 2016. A Review on Shale Reservoirs as an Unconventional Play-The History, Technology Revolution, Importance to Oil and Gas Industry, and the Development Future. *Acta Geologica Sinica* (English edition), 90(5):1887–1902.

Liu, L.F., Wang, Y., Chen, Y.T., Shen, B.J., and Gao, X.Y., 2018. Gas Occurrence and Accumulation Characteristics of Cambrian–Ordovician Shales in the Tarim Basin, Northwest China. *Acta Geologica Sinica* (English edition), 92(5): 1948–1958.

Liu, X.P., Yang, X.L., Zhang, Y.Z., and Han, L., 2008. Application of Spectral Decomposition to Detection of Fracture-Cavity Carbonate Reservoir Beds in the Tahe Oilfield, Tarim Basin, NW China. *Acta Geologica Sinica* (English edition), 82(3):530–536.

Liu, Z.Q., Liu, L., Huang, M., Fei, H.C., Zhou, J., Zhang, Y.X., and Hao, Z.G., 2018. Present Situation of China's Shale Gas Exploration and Development.*Acta Geologica Sinica*(English edition), 92(5):2026 – 2027.

Maxwell, S.C., Rutledge, J., Jones, R., and Fehler, M., 2010. Petroleum reservoir characterization using downhole

microseismic monitoring. *Geophysics*, 75(5): A129–A137.

Meng, X.B., Chen, H.C., Niu, F.L., and Tang, Y.C., 2018. Microseismic Monitoring of Stimulating Shale Gas Reservoir in SW China: 1. An Improved Matching and Locating Technique for Downhole Monitoring. *Journal of Geophysical Research-Solid Earth*, 123(2):1643-1658.

Pei, D.G., Quirein, J.A., Cornish, B. E., and Quinn, D., 2009. Velocity calibration for microseismic monitoring: a very fast simulated annealing (VFSA) approach for joint-objective optimization. *Geophysics*, 74(6):47–55.

Peter, A.G., Kwiseon, K., Wesley, B.J., et al., 2007 Surface passivation optimization using DIRECT. *Journal of Computational Physics*, 224:824–835.

Soledad, R.L., and Danilo, R.V., 2018. Microseismic event location using global optimization algorithms:An integrated and automated workflow. *Journal of Applied Geophysics*, 149:18–24.

Song, F.X., and Toksöz, M. N., 2011. Full-waveform based complete moment tensor inversion and source parameter estimation from downhole micromseismic data for hydrofracture monitoring. *Geophysics*, 76(6):103–116.

Song, W.Q., Qin, X., and Yu, Z.C., 2012. The multi-wave field forward simulation of microseismic based on ray tracing. *Process of geophysics*, 27(4):1501–1508 (in Chinese with English abstract).

Song, W.Q., Zhu, H.W., and Jiang, Y.D., 2013. Bayesian inversion method for surface monitoring microseismic data. *Geophysics prospecting for petroleum*, 52(1):11–16 (in Chinese with English abstract).

Sun, D.S., Chen, Q.C., Wang, Z.X., Zhao, W.H., and Li, A.W., 2015. In Situ Stress Measurement Method and its Application in Unconventional Oil and Gas Exploration and Development. *Acta Geologica Sinica (English edition)*, 89(2):685–686.

Tan, Y.Y., Li, L.L., Zhang, X., and He, C., 2017. An improved method for microseismic source location based on grid search. *Chinese Journal of Geophysics-Chinese Edition*, 60(1): 293–304.

Waldhauser, F., and Ellsworth, W.L., 2000. A double-difference earthquake location algorithm: Method and application to the northern Hayward fault, California. *Bull. Seism. Soc. Am.* 90(6):1353–1368.

Wang, Y.H., 2016. Grid-search method on micro-seismic source fast location based on DIRECT algorithm. *Progress in Geophysics*, 31(4):1700–1708 (in Chinese with English abstract).

Wei, X., Wu, Y.Z., and Chen, L.P., 2012. DIRECT global optimization method using radial basis functions. J. Huazhong Univ. of Sci. & Tech. *(Natural Science Edition)*, 40(5):6–9.

Woo, J.U., Kim, J., and Kang, T.S., 2017. Characteristics in hypocenters of microseismic events due to hydraulic fracturing and natural faults: a case study in the Horn River Basin, Canada. *Geosciences Journal*, 21(5): 683–694.

Yuan, D., and Li, A.B., 2017. Joint inversion for effective anisotropic velocity model and event locations using S-wave splitting measurements from downhole microseismic data. *Geophysics*, 82(3): C133–C143.

Zhang, H.J., and Thunder, C.H., 2003. Double-difference tomography: the method and its application to the Hayward fault, Califomia. Bull. *Seism. Soc. Am*., 93(5):1875–1889.

Zhang, H.J., Sarkar, S., Toksöz, M.N., and Kuleli, H., 2009. Passive Seismic Tomography Using Induced Seismicity at a Petroleum Field in Oman. *Geophysics*, 74(6): WCB57–WCB69.

Zhang, J.W., Zhang, H.J., Zhang, Y.S., and Liu, Q., 2016. Calibrating one-dimensional velocity model for downhole microseismic monitoring using station-pair differential arrival times based on the differential evolution method. *Physics of the Earth and Planetary Interiors*, 261:124–132.

Zhang, X.L., Zhang, F., Li, X.Y., Huang, X.R., and Chen, S.Q., 2013. The influence of hydraulic fracturing on velocity and microseismic location. *Chinese J.Geophys*, 56(10):3552-3560 (in Chinese with English abstract).

Zhao, Y., Yang, T.H., Zhang, P.H., and Zhou, J,R., 2017. The analysis of rock damage process based on the microseismic monitoring and numerical simulations. *Tunnelling and Underground Space Technology*, 69:1–17.

Zhu, H.B., Yang, X.C., and Liao, R.G., 2017. Microseismic fracture interpretation and application based on parameters inversion. *Geophysical Prospecting*, 56(1):150–157.

Zhu, W.X., Zhang, C.X., and Zhang, W.B., 2015. Seismic spectral inversion based on simulated annealing. *Oil geophysical prospecting*, 50(3):495–501, 515.

Zhu, Y.D.Y., Wang, J.L., Sun, F., Lin, J., and Chen, Z.B., 2017. Micro-seismic monitoring and instrument for hydraulic fracturing in the low-permeability oilfield. *Chinese Journal of Geophysics-Chinese Edition*, 60(11): 4282–4293.

Zhuang, D.Y., Ma, K., Tang, C.N., Cui, X., and Yang, G.Q., 2019. Study on crack formation and propagation in the galleries of the Dagangshan high arch dam in Southwest China based on microseismic monitoring and numerical simulation. *International Journal Of Rock Mechanics And Mining Sciences*, 115:157 – 172.

Zou, C.N, Yang, Z., and Zhu, R.K., 2015. Progress in China's Unconventional Oil & Gas Exploration and Development and Theoretical Technologies. *Acta Geologica Sinica* (English edition), 89(3):938–971.

Zou, W., Zhao, G.J., Liu, F., Ye, B., Li, X.H., Huang, T.T., Zhou, Q.M., and Dong, G.L., 2011. Characteristics of Hydrocarbon Accumulation in the Paleozoic Donghetang Formation in the Southwestern Tahe Area. *Acta Geologica Sinica* (English edition), 85(4):899–910.

About the first author

YIN Qifeng, male, born in 1986 in Danyang City, Jiangsu Province; Doctor; graduated from China University of Mining and Technology in 2014; lecturer of Anhui University; He is now interested in the study on microseismic data processing and interpretation, crosshole seismic tomography and background noise imaging. Email: yinqifeng2005@163.com; phone: +86 18110986587.